atmosphere

MDPI

Article

Dual-Pathway Superposition: Independent Forcings of Spring Indian Ocean SST and Summer Tibetan Plateau Heating on Middle and Lower Yangtze Rainfall

Miao Li [1], Yaoming Ma [2,1,3,4,5,6,7,*], Xiaohua Dong [1,8], Mingjing Wang [1], Penghui Yang [1], Qian Zhang [1] and Chengqi Gong [1]

[1] College of Hydraulic & Environmental Engineering, China Three Gorges University, Yichang 443002, China; lim@ctgu.edu.cn (M.L.)
[2] Land-Atmosphere Interaction and Its Climatic Effects Group, State Key Laboratory of Tibetan Plateau Earth System, Environment and Resources (TPESER), Institute of Tibetan Plateau Research, Chinese Academy of Sciences, Beijing 100101, China
[3] China-Pakistan Joint Research Center on Earth Sciences, Chinese Academy of Sciences, Islamabad 45320, Pakistan
[4] College of Earth and Planetary Sciences, University of Chinese Academy of Sciences, Beijing 100049, China
[5] College of Atmospheric Science, Lanzhou University, Lanzhou 730000, China
[6] National Observation and Research Station for Qomolongma Special Atmospheric Processes and Environmental Changes, Shigatse 858200, China
[7] Kathmandu Center of Research and Education, Chinese Academy of Sciences, Beijing 100101, China
[8] Engineering Research Center for the Ecological Environment of the Three Gorges Reservoir Area, Ministry of Education, Yichang 430072, China
* Correspondence: ymma@itpcas.ac.cn

Abstract

The Tibetan Plateau (TP) atmospheric heat source crucially modulates East Asian summer monsoon precipitation, yet its synergy with upstream oceanic signals remains elusive. Using observations (1971–2020) and CMIP6 simulations, we investigate mechanisms coupling the summer TP heating and precipitation over the Middle and Lower Yangtze River (MLYR). SVD analysis reveals a robust positive coupling between them. Mechanistically, TP heating triggers a quasi-stationary Rossby wave train, inducing a "saddle-like" circulation that drives intense MLYR moisture convergence (contributing >90% to precipitation changes). Crucially, we re-examine the upstream oceanic precursor to propose a "dual-pathway superposition" framework. Contrary to the assumed linear causal chain, four-quadrant analysis reveals the spring Indian Ocean Basin Warming (IOBW) and summer TP heating are largely independent drivers (R = 0.24). While IOBW thermodynamically excites an Anomalous Anticyclone supplying abundant MLYR moisture, it lacks robust control over TP heating, which is dominated by internal atmospheric dynamics. However, our findings reveal a critical non-linear synergy: extreme MLYR rainfall strictly requires the coincidental phase overlap of these independent pathways (strong dynamic lifting coupled with oceanic moisture). CMIP6 simulations corroborate this independence, further emphasizing that extreme MLYR rainfall results from phase superposition rather than a single causal chain.

Keywords: Tibetan Plateau atmospheric heat source; Middle and Lower Yangtze River; rossby wave train; Indian Ocean basin warming; non-linear superposition; internal atmospheric variability; CMIP6

Academic Editor: Tin Lukić

Received: 2 March 2026
Revised: 15 April 2026
Accepted: 15 April 2026
Published: 18 April 2026

1. Introduction

The Tibetan Plateau (TP), as the highest and most topographically complex thermal forcing source on Earth, exerts a profound influence on the atmospheric circulation and climate systems over East Asia and even the globe [1–4]. In summer, acting as a colossal elevated heat source, the TP heats the middle and upper troposphere through the Sensible Heat Air Pump (SHAP) and intense condensation latent heat release [5]. This process not only drives the onset and maintenance of the East Asian Summer Monsoon (EASM) [6], but also propagates energy upstream and downstream by exciting atmospheric waves [7]. The Middle and Lower Reaches of the Yangtze River (MLYR), located downstream of the TP, is a key region for the EASM rain belt, and its summer precipitation anomalies are directly related to China's socio-economic development and ecological security [8]. Numerous observational and modeling studies have confirmed a close teleconnection between the interannual variability of the TP atmospheric heat source and the summer drought-flood patterns in the MLYR [9,10]. Specifically, recent extreme precipitation events, such as the record-breaking persistent extreme Meiyu rainfall in 2020, have been closely linked to the anomalous intensification of the TP thermal forcing [11–13].

However, under the new climate background, this classic "TP-Yangtze" teleconnection mechanism faces new challenges. First, driven by global warming, the TP is undergoing a rapid "warming and wetting" process [14–16]. Previous studies have indicated that the TP atmospheric heat source has shown an overall weakening trend since the end of the 20th century, which is mainly attributed to the significant decrease in surface sensible heat flux [17,18]. Against the backdrop of continuous warming and wetting over the TP [19], whether the internal structure of the heat source has shifted from being sensible heat-dominated to latent heat-dominated, and whether the intensity of the heat source has experienced a trend reversal from weak to strong after the entry into the 21st century [20,21], remains to be further clarified. Has this potential structural shift altered the key regions and physical pathways through which the TP heat source affects the downstream areas? Second, the dynamic mechanisms by which TP thermal forcing affects downstream regions are extremely complex. In addition to the traditional local thermal regulation of the South Asian High (SAH) and the Western Pacific Subtropical High (WPSH) [2,22], the quasi-stationary Rossby wave train (e.g., the "Silk Road Pattern", SRP) excited by the TP acting as a wave source and propagating along the westerly jet is considered a more dominant pathway for remote modulation [23–26]. However, how strong heat source anomalies systematically reshape the high, middle, and low-level circulation configurations through specific wave train structures, and particularly how they dominate the dynamic term's contribution in the moisture budget, requires further quantitative diagnosis.

Furthermore, as a short-memory system, the maintenance of interannual anomalies in the atmosphere often relies on external oceanic forcing with long "memory". Tropical Indian Ocean Sea Surface Temperature (SST) typically exhibits an Indian Ocean Basin Warming (IOBW) during the summer of El Niño decaying years and modulates East Asian climate cross-seasonally through the famous "Indian Ocean Capacitor (IOC)" effect [27]. Previous studies have pointed out that the warming of the Indian Ocean can not only directly affect the East Asian monsoon circulation by exciting an Anomalous Anticyclone (AAC) over the Northwest Pacific [28,29], but also modulates the circulation and thermal conditions around the TP. On the one hand, it can strengthen the SAH over the TP by altering the atmospheric thermal structure [30]; on the other hand, it can increase precipitation and latent heat release over the TP by enhancing moisture transport to the plateau [29]. To further deepen our understanding of this complex Ocean–Plateau–Atmosphere interaction, it is essential to explore the specific dynamic pathways beyond the linear chain perspective. Given that the TP's thermal variability is also governed by internal atmospheric dynamics,

a critical question arises: Do the spring IOBW and the summer TP heat source act as largely independent forcings on interannual timescales? If so, how do the thermodynamic moisture pathway (ocean-driven) and the dynamic lifting pathway (plateau-driven) synergistically superimpose to trigger extreme flooding over the MLYR? To address these fundamental questions, this study utilizes multi-source observations (1971–2020) alongside CMIP6 AMIP simulations [31–33] to rigorously investigate these relationships, aiming to propose a novel "Dual-Pathway Superposition" framework.

2. Materials and Methods

2.1. Study Area

This study focuses on two core geographical units, the TP and the MLYR, regarding them as the atmospheric heat source forcing region and the climate response region, respectively. Their geographical locations and topographic features are illustrated in Figure 1. Specifically, the research domain for the TP is selected as 25°48′ N–39°97′ N, 75°87′ E–105°69′ E. With an average elevation exceeding 4000 m and complex, steep terrain, this region is known as the "Roof of the World" and the "Third Pole." As the highest and most extensive topographic unit globally, the TP evolves into a colossal heat source extending into the middle troposphere during summer through the powerful SHAP effect and intense condensation latent heat release, thereby exerting significant thermal forcing on the atmospheric circulation over East Asia and even the globe [1,34]. As the key downstream region influenced by TP thermal forcing, the MLYR (defined here as 24°49′ N–34°20′ N, 106°09′ E–121°90′ E) is characterized by low-lying flat terrain and dense river networks, covering numerous lakes such as Poyang Lake and Dongting Lake. Located in a typical subtropical monsoon climate zone, this region is primarily controlled by the EASM during summer and receives abundant moisture transport. It serves not only as the concentrated area for Meiyu frontal precipitation but also as a region highly sensitive and prone to drought and flood disasters [8].

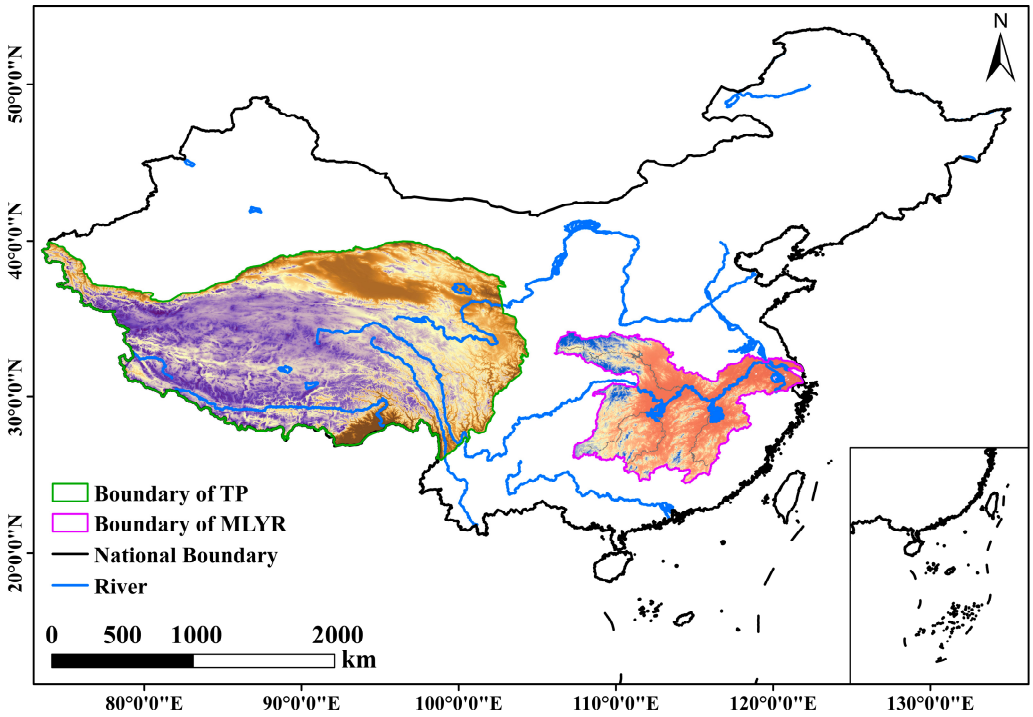

Figure 1. Overview of the study area: Topography and geographical location of the TP and the MLYR.

2.2. Data Sources

To ensure the reliability of the conclusions through multi-source cross-validation, this study utilizes a comprehensive set of data, including high-resolution atmospheric reanalysis datasets, station-based gridded observations, SST data, and numerical model outputs. A summary of the primary datasets used in this study is provided in Table 1.

Table 1. Summary of datasets used in this study.

Data Type	Dataset Name	Source	Spatial Resolution	Time Period
Atmospheric Reanalysis	ERA5	ECMWF	0.25° × 0.25°	1971–2020
Precipitation Observation	CN05.1	CMA	0.25° × 0.25°	1971–2020
Sea Surface Temperature	ERSST v5	NOAA	2° × 2°	1971–2020
Numerical Model	CMIP6 AMIP *	WCRP	1.125° × 1.125° **	1979–2014

* CMIP6 AMIP refers to the Multi-Model Ensemble (MME) constructed from three models: BCC-CSM2-MR, CESM2, and MRI-ESM2-0. ** Represents the grid resolution after unified interpolation.

Detailed descriptions of each dataset are provided below:

1. Atmospheric Reanalysis Data:

The fifth-generation global atmospheric reanalysis (ERA5) released by the European Centre for Medium-Range Weather Forecasts (ECMWF) is employed [35]. The selected data period spans from 1971 to 2020. To capture the local thermal features over the complex terrain of the TP and the fine-scale circulation structure over the MLYR, the high spatial resolution version of 0.25° × 0.25° is selected. Benefiting from the advanced 4D-Var data assimilation system, ERA5 demonstrates excellent applicability in describing atmospheric thermodynamic fields and water vapor content over the TP region. Multiple evaluation studies have confirmed that it is currently one of the highest-quality reanalysis datasets available [36,37].

2. Precipitation Observation Data:

The CN05.1 gridded observation dataset provided by the National Climate Center of the China Meteorological Administration (CMA) is used [38]. This dataset is constructed based on daily observations from over 2400 stations across China, with a horizontal resolution of 0.25° × 0.25°. It can precisely characterize the spatial distribution details of precipitation over the MLYR.

3. Sea Surface Temperature Data:

The monthly mean Extended Reconstructed Sea Surface Temperature version 5 (ERSST v5) dataset provided by the National Oceanic and Atmospheric Administration (NOAA) is adopted [39], with a horizontal resolution of 2.0° × 2.0°.

4. CMIP6 AMIP Model Data:

Data from the Atmospheric Model Intercomparison Project (AMIP) experiments within the Coupled Model Intercomparison Project Phase 6 (CMIP6) are selected [40]. Three mainstream models (BCC-CSM2-MR, CESM2, and MRI-ESM2-0) that exhibit good performance in simulating the East Asian monsoon are chosen for this study. These specific models were chosen because multiple comprehensive evaluation studies have confirmed their superior performance and relative structural independence in simulating the EASM and the Northwest Pacific circulation systems [31,41]. To facilitate the MME analysis, the data from each model were regridded to a uniform 1.125° × 1.125° grid using the bilinear interpolation method. Although regridding CMIP6 models to a relatively coarser resolution may smooth out certain localized topographic precipitation extremes captured by the high-resolution observations (i.e., ERA5 and CN05.1), it does not compromise the reliability of the MME in

this study. The core physical mechanisms investigated here—specifically the large-scale AAC over the Northwest Pacific and the quasi-stationary Rossby wave train—operate on synoptic to planetary scales. For such large-scale atmospheric circulation configurations, the MME approach effectively filters out unforced internal noise and robustly extracts the oceanic-forced dynamic responses, ensuring a highly reliable comparative analysis with observational facts.

2.3. Research Methodologies

2.3.1. Calculation of Atmospheric Heat Source

This study adopts the direct method to calculate the atmospheric heat source (Q_1) over the TP [42]:

$$Q_1 = SH + LH + R_{net} \tag{1}$$

The individual components were sourced and calculated as follows:

Surface Sensible Heat Flux (SH): This component was directly obtained from the ERA5 reanalysis dataset, which provides high-quality, pre-calculated surface flux products.

Latent Heat Flux (LH): This component, representing the energy released by condensation from precipitation, was independently calculated using the formula:

$$LH = P_r \times L_W \times \rho \tag{2}$$

where P_r is the precipitation rate; L_w is the latent heat coefficient of condensation for water, taken as 2.5×10^6 J/kg; and ρ is the density of water, taken as 1.0×10^3 kg/m^3. The LH is typically inversely derived from precipitation data.

Net Radiation Flux (R_{net}): The net radiation flux of the atmospheric column was also independently calculated based on the four fundamental radiation variables from ERA5:

$$R_{net} = S_{net}^{top} - S_{net}^{sfc} + L_{net}^{top} - L_{net}^{sfc} \tag{3}$$

where S and L represent shortwave radiation and longwave radiation, respectively. The superscripts top and sfc denote the top of the atmosphere and the surface, respectively. The units of all calculated results are unified to W/m^2.

2.3.2. Moisture Budget Equation and Linear Decomposition

Precipitation anomalies (P') are primarily determined by the anomalies of vertically integrated moisture flux divergence. Neglecting the minor contributions from evaporation anomalies and nonlinear terms, this term can be linearly decomposed into a dynamic term and a thermodynamic term [43]:

$$P' \approx -\frac{1}{g}\int_{P_s}^{P_{top}} \nabla\cdot(\overline{q}V')dp - \frac{1}{g}\int_{P_s}^{P_{top}} \nabla\cdot(q'\overline{V})dp \tag{4}$$

where the overbar ($^-$) denotes the climatological mean state, and the prime ($'$) denotes the anomaly state. The first term on the right-hand side is the dynamic term, reflecting the change in moisture convergence caused by wind field anomalies (V'); the second term is the thermodynamic term, reflecting the change in moisture convergence caused by specific humidity anomalies (q').

2.3.3. Statistical Diagnostic Methods

To investigate the coupling characteristics and physical mechanisms, this study employs a suite of statistical diagnostic methods. Singular Value Decomposition (SVD) [44] is utilized to identify the dominant coupled modes between the TP heat source and MLYR

precipitation. Composite analysis, with its statistical significance evaluated by Welch's *t*-test [45], is conducted to extract the circulation and moisture anomalies associated with typical years. Furthermore, a four-quadrant composite analysis is introduced to rigorously quantify the non-linear superposition effects between different forcing sources.

To focus strictly on interannual variability, linear detrending was performed on all time series and gridded field data prior to any statistical analysis.

2.3.4. Index Definition

To quantify the key forcing signals, two primary indices are utilized in this study.

(1) Key Region Heat Source Index: This index is constructed to represent the thermal forcing from the identified key region of the southeastern TP (89° E–103° E, 27° N–34° N). It is calculated by taking the area-weighted (cosine latitude-weighted) average of the summer (June-July-August) atmospheric heat source anomalies within this domain.

(2) Spring IOBW Index: This index is constructed to represent the thermodynamic forcing from the tropical Indian Ocean. First, the monthly mean SST anomalies are calculated for the spring season (March-April-May). Then, an area-weighted (cosine latitude-weighted) average is computed over the tropical Indian Ocean basin, defined as the region 20° S–20° N, 40° E–100° E.

3. Results

3.1. Coupling Modes Between Summer TP Atmospheric Heat Source and MLYR Precipitation and Identification of Key Regions

To objectively identify the dominant coupling characteristics between the summer atmospheric heat source over the TP and precipitation over the MLYR from spatial fields, this study applied the SVD method to the standardized anomaly fields of both variables for the period 1971–2020. The squared covariance fraction (SCF) of the first SVD mode reaches as high as 60.29%, dominating the total covariance variability. This indicates that this mode effectively represents the primary interaction relationship between the two fields.

Figure 2 illustrates the spatiotemporal distribution characteristics of this coupling mode. In terms of spatial distribution, the homogeneous correlation field of the TP heat source (Figure 2a) exhibits a significant "east–west out-of-phase" pattern. The center of high positive correlations is highly concentrated over the southeastern TP, geographically covering the Hengduan Mountains and the middle and lower reaches of the Yarlung Tsangpo River. Correspondingly, the heterogeneous correlation field of MLYR precipitation (Figure 2b) is characterized predominantly by positive correlations. The significant high-correlation zone is distributed in a band shape along the mainstream of the MLYR and extends southward to the Dongting Lake and Poyang Lake basins. This spatial configuration reveals a clear teleconnection pattern: when the heat source over the southeastern TP is anomalously strong, precipitation over the main rain belt of the MLYR tends to increase significantly. Furthermore, the time coefficients (PC1) of this mode exhibit highly synchronous variations (Figure 2c), with a correlation coefficient of 0.601 ($p < 0.001$). Notably, extreme positive anomalies are observed during typical flood years such as 1998 and 2020. Statistically, this suggests that the atmospheric heat source over the southeastern TP is a key forcing factor driving the interannual variability of precipitation over the MLYR.

Given that the SVD analysis reveals the spatial inhomogeneity of the influence of the TP heat source, and to characterize this key forcing signal in a convenient and physically meaningful manner, the region of 89° E–103° E, 27° N–34° N is defined as the "TP heat source key region" (indicated by the green dashed box), based on the distribution of high-loading zones in the SVD left field (Figure 2a). From a physical and climatological perspective, the dominance of the southeastern TP is theoretically well-founded. Unlike

the western TP, which is relatively dry and primarily dominated by shallow surface sensible heating during summer, the southeastern TP acts as a major convergence zone for abundant moisture transported by the Asian summer monsoon. This strong local moisture convergence triggers intense deep convection and massive condensation latent heat release. Dynamically, such deep latent heating is highly efficient at warming the middle and upper troposphere, thereby serving as a powerful wave source to excite the downstream quasi-stationary Rossby wave train. Consequently, the southeastern TP exerts a substantially greater influence on the East Asian summer climate than its western counterpart. To verify its reliability, the summer heat source index averaged over this key region is compared against the SVD-PC1. The results in Figure 3 show that the temporal variations in the two series have been highly consistent over the past 50 years, with a correlation coefficient as high as 0.915 ($p < 0.001$). This indicates that the simple key region average index can explain over 83% of the variance of the dominant SVD mode, demonstrating excellent representativeness. Therefore, in the subsequent diagnosis of physical mechanisms, this "Key Region Heat Source Index" will be consistently adopted as the core metric to quantify the intensity of TP thermal forcing.

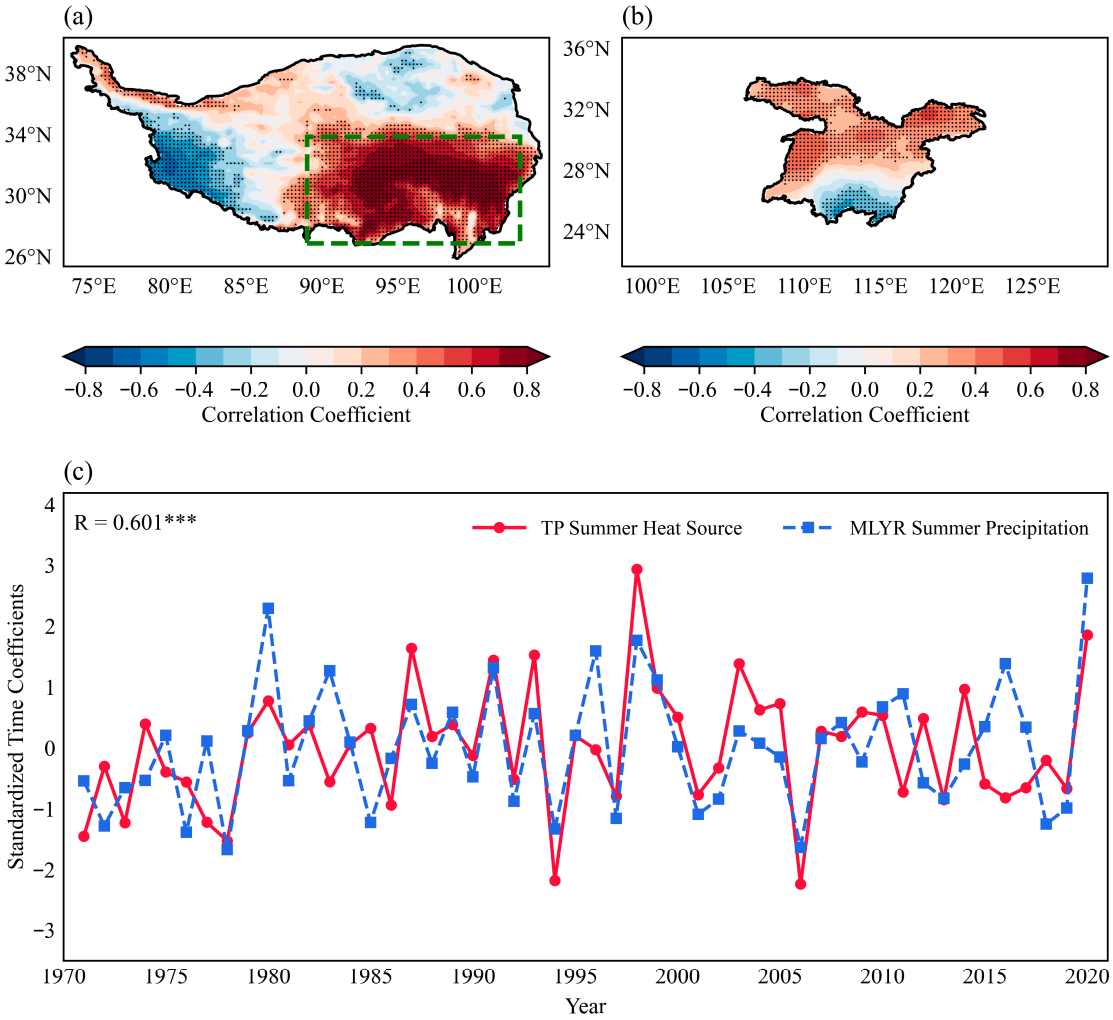

Figure 2. Spatiotemporal characteristics of the first SVD mode for the summer atmospheric heat source over the TP and precipitation in the MLYR. (**a**) Homogeneous correlation map of the TP heat source (the green dashed box indicates the key region). (**b**) Heterogeneous correlation map of MLYR precipitation. (**c**) Standardized time series of the first SVD mode. The stippled areas indicate statistical significance at the 95% confidence level, and the *** denote that the correlation coefficient is statistically significant at the 99.9% confidence level.

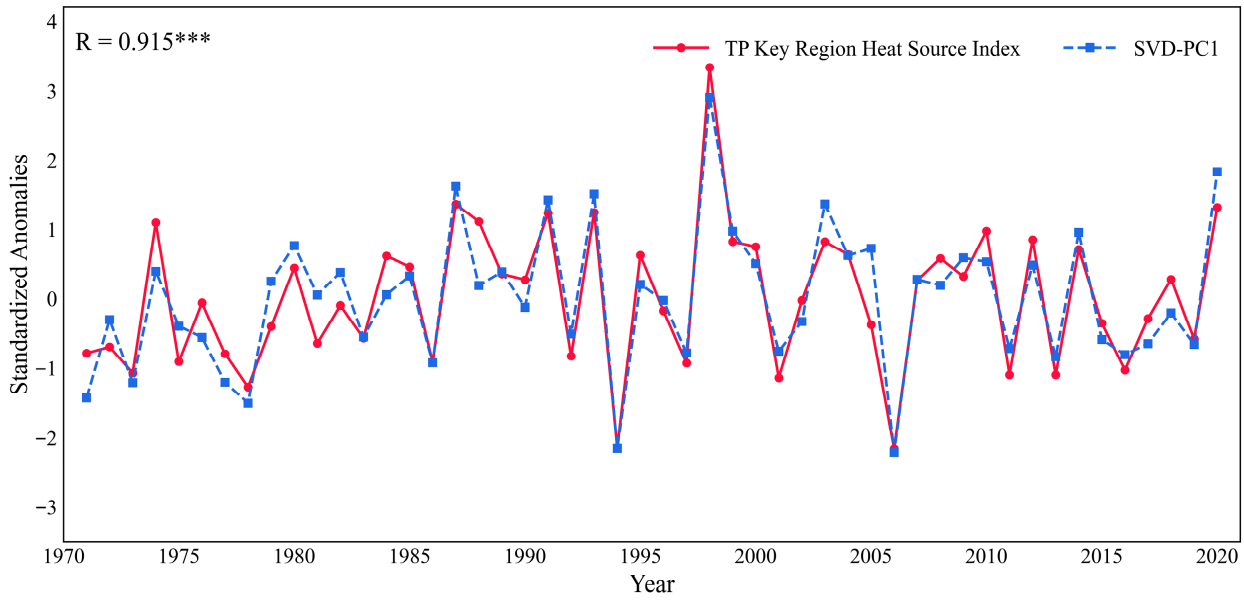

Figure 3. Comparison between the standardized TP key region heat source index and the SVD-PC1 time series. The *** denote that the correlation coefficient is statistically significant at the 99.9% confidence level.

3.2. Anomalies of Atmospheric Circulation and Diagnosis of Dynamic Mechanisms

To reveal the dynamic pathways through which TP heat source anomalies affect precipitation over the MLYR, a composite analysis was performed based on the key region heat source index. Figure 4 illustrates the circulation anomalies in the upper and middle troposphere during strong heat source years, depicting the adjustment process of the large-scale circulation background.

First, in the upper troposphere (200 hPa), Figure 4a reveals a quasi-stationary Rossby wave train propagating eastward along the westerly jet waveguide. This wave train exhibits a typical "cyclone–anticyclone–cyclone" alternating phase structure over the Eurasian continent. Specifically, the anticyclonic anomaly over the TP is superimposed onto the climatological SAH, resulting in the strengthening and eastward extension of the SAH (indicated by the red solid line). Influenced by this configuration, the MLYR is situated precisely in the strong divergence region ahead of the upper-level anticyclonic ridge, with the central divergence anomaly exceeding 2.0×10^{-6} s^{-1}. This intense "upper-level dynamic pumping" effect provides a crucial background of ascending motion for the maintenance of deep convection.

Modulated by the energy dispersion of the upper-level wave train, the circulation in the middle troposphere (500 hPa) also exhibits a significant response. As shown in Figure 4b, a distinct "Northern Trough and Southern Ridge" dipole pattern forms over East Asia: the East Asian Trough at middle and high latitudes deepens significantly, steering dry and cold air southward; meanwhile, the WPSH strengthens and extends westward significantly (Figure 4c). This anomalously westward-extended WPSH creates a convergence zone with the southward-moving cold air over the MLYR. Simultaneously, the airflow on the western flank of the WPSH steers a large amount of warm and moist air northward, providing abundant water vapor conditions for precipitation.

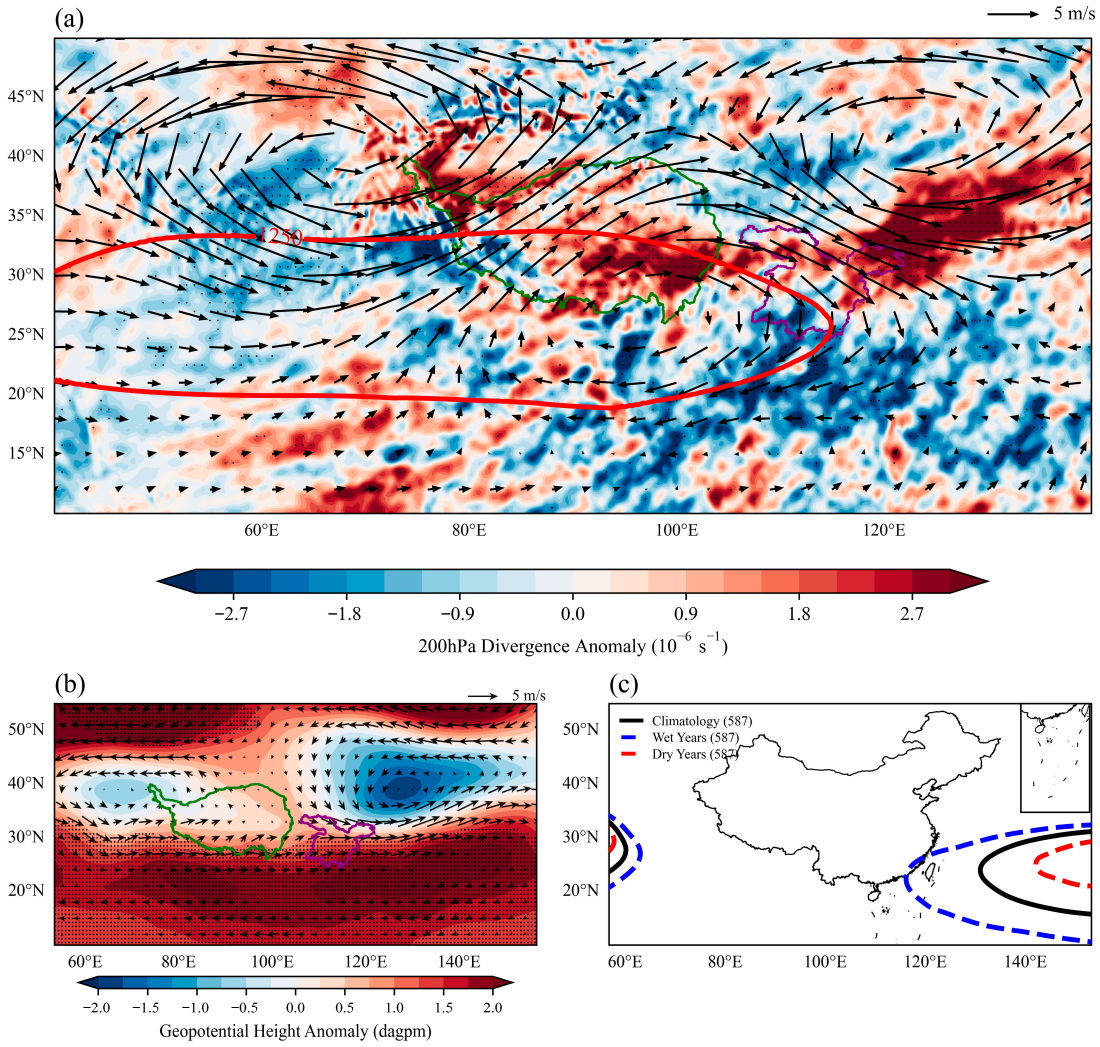

Figure 4. Composite anomalies of atmospheric circulation in the upper and middle troposphere between strong and weak heat source years. (**a**) 200 hPa divergence anomalies (shading; 10^{-6} s^{-1}) and wind anomalies (vectors). The red solid line indicates the climatological boundary of the South Asian High (1250 dagpm). (**b**) 500 hPa geopotential height anomalies (shading; dagpm) and wind anomalies. (**c**) Comparison of the WPSH characteristic contour (587 dagpm). The stippled areas indicate statistical significance at the 95% confidence level. ("Wet Years" and "Dry Years" represent the strong and weak TP heat source years, respectively. These years are strictly identified based on the standardized TP key region heat source index exceeding +1.0 and falling below −1.0 standard deviations).

The lower-tropospheric circulation responds significantly to the aforementioned upper-level forcing, establishing an efficient water vapor "transport corridor." Figure 5 illustrates the moisture dynamic processes at 850 hPa. Driven by the westward extension of the 500 hPa WPSH, an AAC appears over the region from the South China Sea to the Northwest Pacific. On its northwestern flank, an anomalously strong low-level southwesterly jet is established (Figure 5d). Notably, the direction of this anomalous jet is highly consistent with the direction of the climatological mean summer water vapor transport (Figure 5c). The superposition of the two generates a "relay acceleration" effect, continuously transporting abundant water vapor from the Indian Ocean and the South China Sea to the MLYR, leading to a significant increase in specific humidity in this region (Figure 5a). Finally, under the synergistic effect of dynamic convergence and upper-level divergence, the large amount of transported moisture converges and ascends over the MLYR, triggering deep vertical ascending motion (Figure 5b), thereby resulting in an anomalous increase in precipitation.

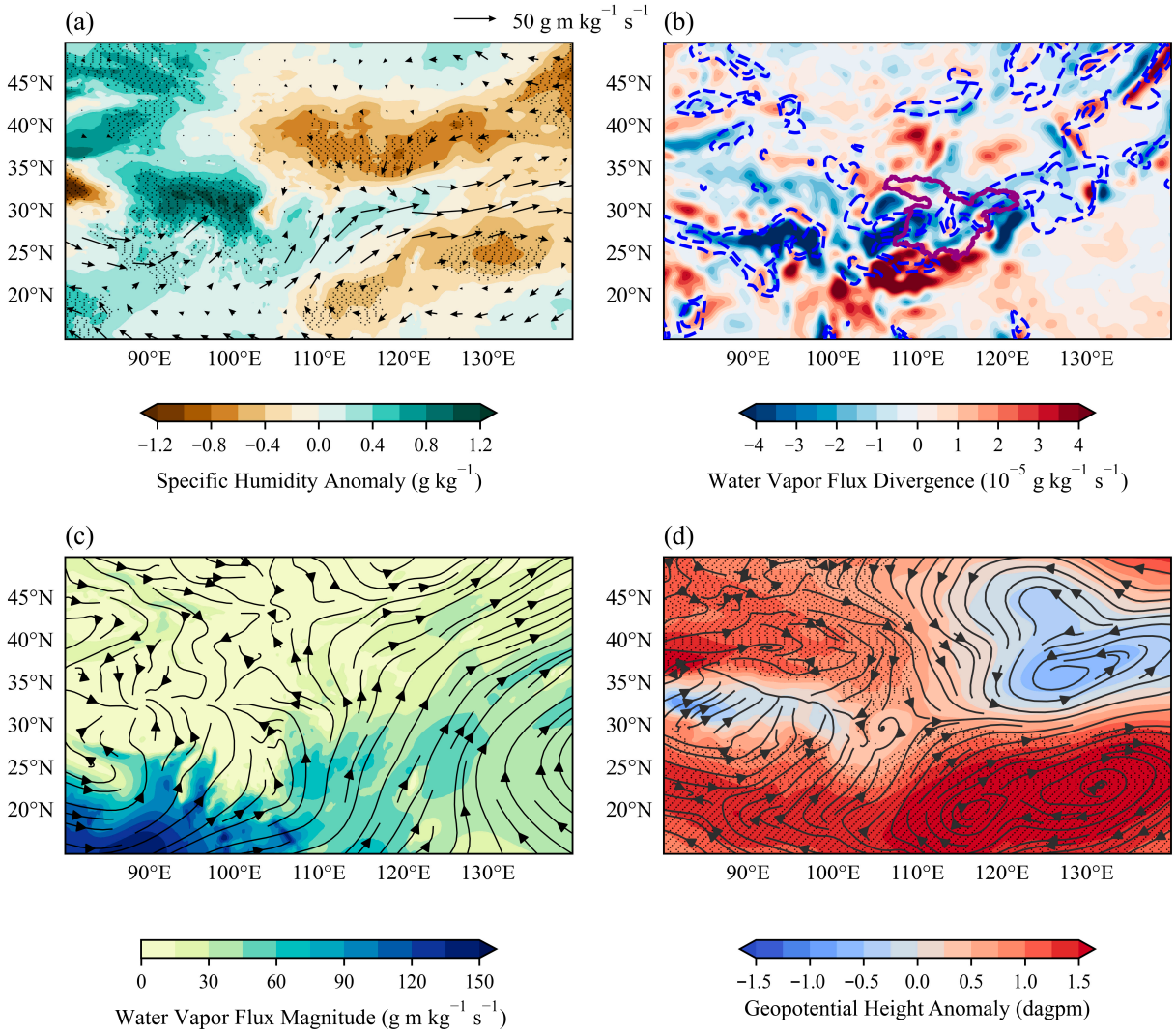

Figure 5. Composite anomalies of moisture and dynamic fields at 850 hPa in strong heat source years. (**a**) Specific humidity anomalies (shading; g kg^{-1}) and moisture flux anomalies (vectors; g m kg^{-1} s^{-1}). (**b**) Moisture flux divergence anomalies (shading; 10^{-5} g kg^{-1} s^{-1}) and vertical velocity anomalies (blue dashed lines indicate ascent). (**c**) Climatological summer moisture transport (vectors) and flux magnitude (shading; g m kg^{-1} s^{-1}). (**d**) 850 hPa geopotential height anomalies (shading; dagpm) and wind anomalies (streamlines). The stippled areas indicate statistical significance at the 95% confidence level.

To further elucidate the relative importance of dynamic factors (circulation anomalies) and thermodynamic factors (moisture content anomalies) in the aforementioned process, this study quantitatively decomposed the precipitation anomalies using the moisture budget equation. Figure 6 illustrates the relative contribution of each term. The results indicate that the total moisture budget anomaly over the MLYR during strong heat source years is +1.31 mm day^{-1}. Specifically, the "dynamic term" induced by wind field anomalies contributes as much as 1.20 mm day^{-1}, accounting for 91.6% of the total anomaly, whereas the "thermodynamic term" induced by specific humidity anomalies contributes only 8.4%. This significant disparity in proportions reveals that, although atmospheric humidity has increased, the adjustment of atmospheric circulation patterns (i.e., the intensification of the southwesterly jet and convergent ascent induced by the Rossby wave train) is the decisive mechanism leading to the increased summer precipitation over the MLYR, rather than the thermodynamic moistening effect alone.

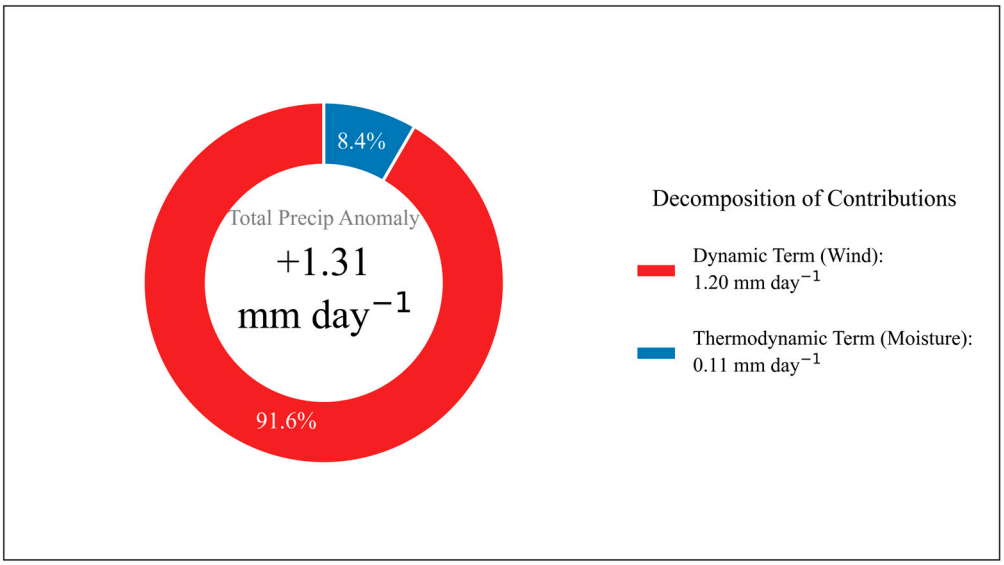

Figure 6. Quantitative attribution of precipitation anomalies in the MLYR based on the moisture budget diagnosis.

3.3. The Ambiguous Oceanic Precursor and Dual-Pathway Superposition

To explore the external forcing source driving the MLYR precipitation, previous studies often focused on the cross-seasonal persistent signals of global SST. Figure 7 displays the lag correlation between the spring IOBW index and the summer atmospheric fields. While Figure 7b reveals that the spring warm SST excites a strong AAC over the Northwest Pacific, establishing a southwesterly moisture transport tendency, the correlation pattern between IOBW and the TP heat source (Figure 7a) is spatially inhomogeneous, with positive signals largely confined to the southeastern edge. This distribution suggests that the relationship between the spring IOBW and the summer TP heat source involves nuanced interactions, warranting a further quantitative investigation into their independence and potential synergistic effects.

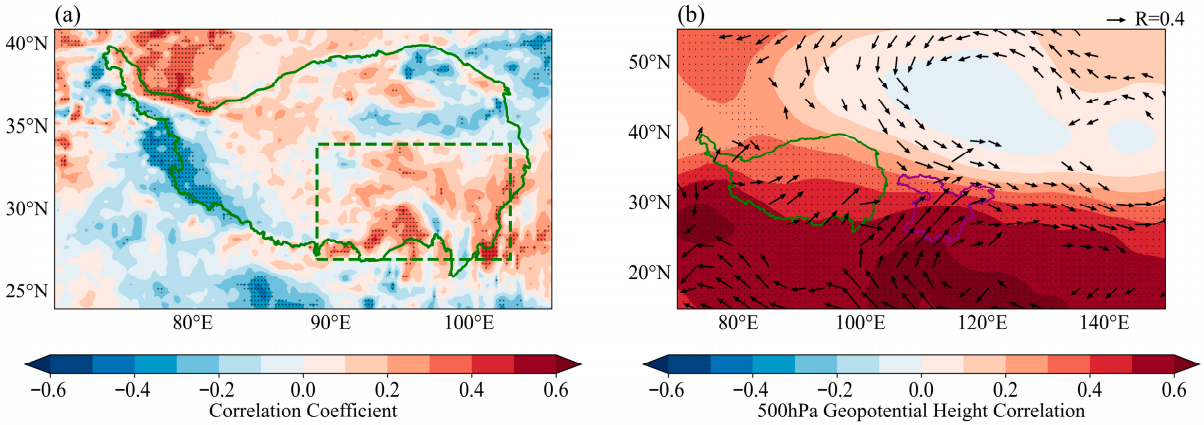

Figure 7. Observed lag correlations between the spring IOBW index and summer atmospheric anomalies. (**a**) Spatial distribution of the correlation with the summer TP atmospheric heat source. (the green dashed box indicates the heat source key region). (**b**) Correlation with the summer 500 hPa geopotential height and 850 hPa wind field, illustrating the IOBW-excited AAC and moisture transport tendency. The stippled areas indicate statistical significance at the 95% confidence level.

A four-quadrant composite analysis (Figure 8) is employed to rigorously quantify the exact causal links and their synergistic impact on MLYR precipitation. In this analysis, the 500 hPa vertical velocity over the TP key region serves as a proxy for the heating-induced

dynamic lifting, directly capturing the dynamic consequence of the TP thermal forcing. Concurrently, the moisture convergence strictly within the MLYR geographical boundaries is utilized as a robust proxy for precipitation. First, the scatter plot (Figure 8a) reveals a very weak correlation (R = 0.24) between the Spring IOBW index and the Summer TP dynamic proxy. This quantitatively confirms that the remote SST is not the dominant driver of TP heating; instead, they act as largely independent drivers, with the TP heat source likely being governed by internal mid-latitude atmospheric variability.

More importantly, Figure 8b unveils a non-linear superposition effect. Extreme moisture convergence over the MLYR requires the coincidental phase overlap of these two independent pathways. When the TP heat source provides dynamic lifting (Rossby waves) and the IOBW concurrently provides abundant moisture via the AAC (Quadrant 1: Dual-High), the moisture convergence is drastically enhanced (+0.48 Std). Strikingly, if only the TP dynamic lifting is present without oceanic moisture (Quadrant 2), or only moisture is transported without TP dynamic lifting (Quadrant 3), the convergence anomaly is either neutral (−0.07 Std) or significantly negative (−0.37 Std). This proves that dynamic lifting without moisture, or moisture without dynamic lifting, inherently fails to produce extreme rainfall events.

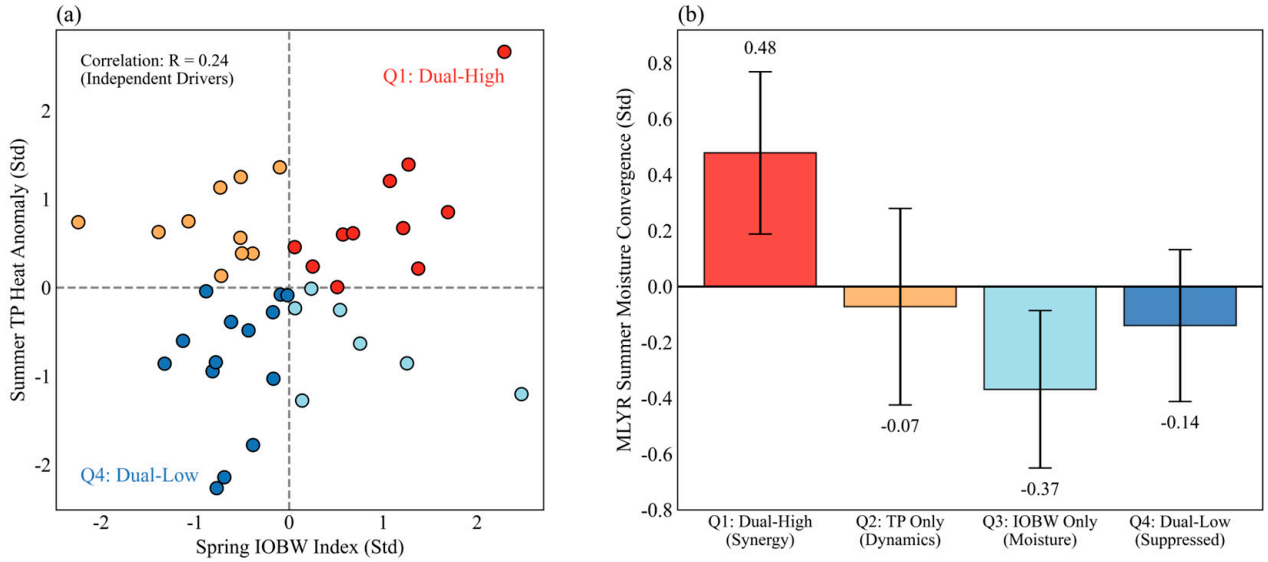

Figure 8. Four-quadrant composite analysis quantifying the independence and non-linear superposition effect. (**a**) Scatter plot of the standardized Spring IOBW index (moisture proxy) versus the Summer TP heat proxy (500 hPa vertical velocity). (**b**) The standardized MLYR summer moisture convergence anomalies composited for each of the four quadrants. Colors correspond to the four specific quadrants (Q1–Q4), linking the individual years in (**a**) with their respective composite means in (**b**).

Finally, we re-evaluated this nuanced mechanism using the CMIP6 AMIP MME. As shown in Figure 9, the models successfully reproduce the summer AAC and the southwesterly wind anomalies (the thermodynamic moisture pathway) driven by Indian Ocean warming (Figure 9b). However, most models struggle to capture a robust, positive response of the TP heat source to the IOBW forcing (Figure 9a). To quantitatively evaluate this, we extracted the simulated summer precipitation over the TP key region—serving as a robust proxy for the condensation-dominated latent heat source—and analyzed its correlation with the observed spring IOBW index. As illustrated in the scatter plot (Figure 9c), the relationship is exceptionally weak and not statistically significant (R = 0.06). Rather than being a mere systematic bias, this modeling result actually corroborates our observational finding: the interannual variability of the TP heat source is fundamentally dominated

by internal atmospheric dynamics, which are inherently difficult to predict via remote oceanic boundaries. Therefore, the "synergy" is physically manifested as the coincidental spatial superposition of the ocean-driven moisture pathway and the plateau-driven dynamic pathway.

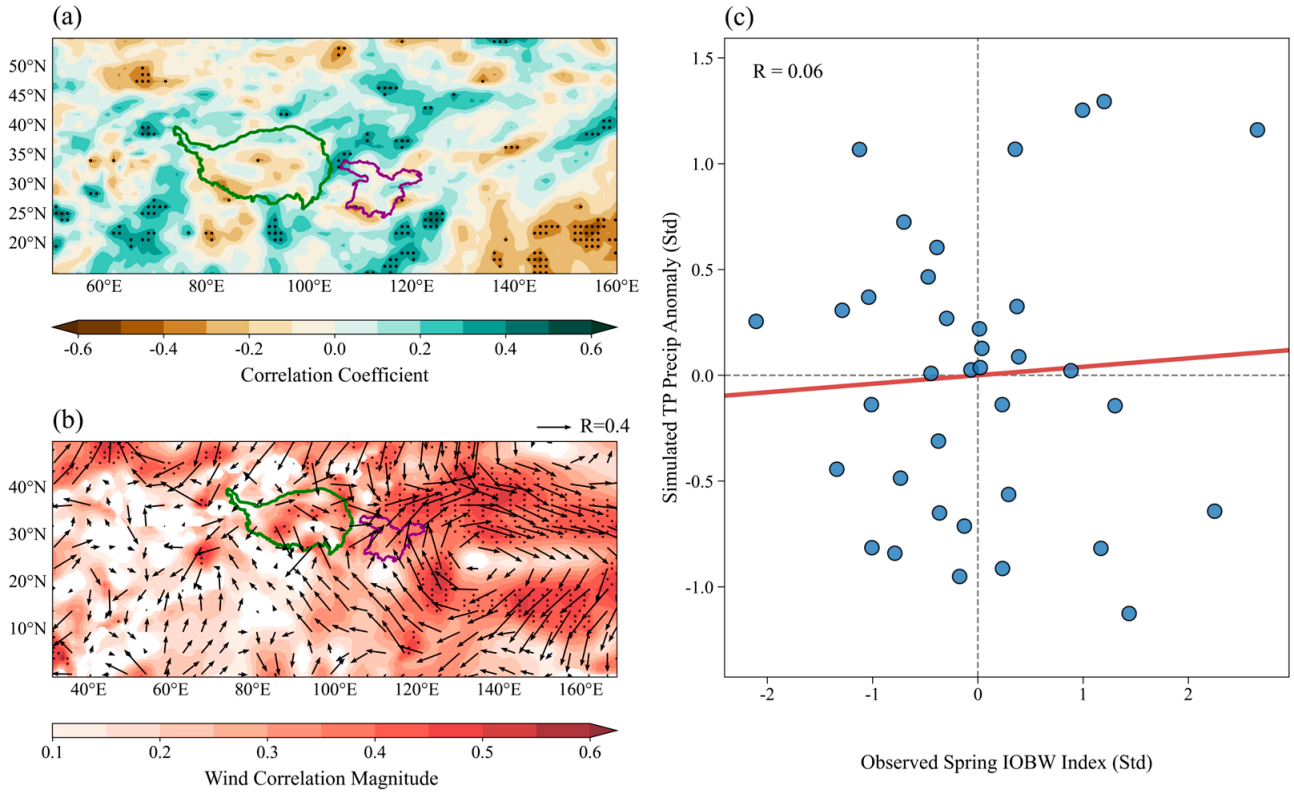

Figure 9. Verification of the oceanic forcing on atmospheric circulation using the CMIP6 AMIP MME. (**a**) Simulated lag correlation between the spring IOBW index and summer precipitation. (**b**) Simulated lag correlation with the summer 850 hPa wind field. (**c**) Correlation analysis between the observed spring IOBW index and the simulated summer precipitation over the TP key region, where the solid red line represents the linear regression fit. The stippled areas indicate statistical significance at the 95% confidence level.

4. Discussion

Through observational diagnostics and CMIP6 numerical simulations, this study refines our understanding of how remote oceanic forcing and inland plateau heating jointly affect MLYR precipitation. Rather than relying solely on the traditional perspective of sequential causal chains, this paper verifies the direct moisture regulation of the IOC effect on the East Asian circulation [27], while further clarifying the relatively independent role of the southeastern TP.

Specifically, previous studies [29] have provided valuable insights into the potential thermodynamic link between the IOBW and the TP. Building upon these foundations, our current analysis (Figure 8a) and CMIP6 evaluations (Figure 9) suggest that on interannual timescales, the relationship manifests as a complex interaction rather than a simple linear drive. This indicates that the TP heat source is not solely dependent on oceanic signals but is also significantly modulated by chaotic internal atmospheric variability [46,47], such as mid-latitude transient eddy activities, as well as complex local land-surface feedbacks including soil moisture-precipitation coupling [48] and snow albedo effects [49].

Recognizing the independence of these two forcing sources, we propose a "Dual-Pathway Superposition" framework. The TP heating dynamically excites a middle-upper

tropospheric Rossby wave train, which shares characteristics with the "SRP" [24], establishing a "Northern Trough and Southern Ridge" pattern favorable for dynamic lifting. Simultaneously, the Spring IOBW thermodynamically sustains the AAC, providing a massive moisture transport pathway. The discovery of this non-linear superposition provides a far more refined and scientifically rigorous explanatory framework for extreme floods in the MLYR during El Niño decaying years, such as 1998 and 2020. It corroborates the view that extreme events like the 2020 record-breaking persistent extreme Meiyu rainfall require the coincidental overlap of concurrent multi-factor forcings [8,50].

Finally, the systematic southward bias of the rain belt in CMIP6 AMIP simulations [41] further highlights the challenges current models face in capturing internal variability over complex terrain. Future studies should expand the research scope from the seasonal mean scale to the sub-seasonal scale (e.g., MJO) to clarify the specific transient modulation processes of TP heat source fluctuations on the phase changes in Meiyu precipitation [51].

5. Conclusions

Using multi-source observational data and CMIP6 AMIP MME simulation data, this study investigated the mechanisms driving summer precipitation over the MLYR, focusing on the distinct roles of the TP atmospheric heat source and spring Indian Ocean SST. The main conclusions are as follows:

1. A robust positive coupling exists between the enhancement of the atmospheric heat source over the southeastern TP and the increase in summer precipitation over the MLYR.
2. The Dynamic Pathway: Strong TP heat source anomalies, largely driven by internal atmospheric dynamics, excite a quasi-stationary Rossby wave train propagating along the westerly jet. This induces a saddle-like circulation pattern characterized by a deepened East Asian Trough and a westward-extended WPSH, providing intense upper-level divergence and dynamic lifting over the MLYR. Quantitative moisture budget diagnosis confirms that such circulation-induced dynamic anomalies overwhelmingly dominate the extreme precipitation, contributing over 90% to the total moisture convergence.
3. The Thermodynamic Pathway and Non-linear Superposition: The spring IOBW serves as an independent external forcing. Persisting into summer, it excites an AAC over the Northwest Pacific, directly establishing a robust southwesterly moisture transport corridor to the MLYR. Crucially, extreme MLYR precipitation is not driven by a linear ocean-to-plateau causal chain, but rather depends on the non-linear superposition of these two independent pathways. Single forcing (only moisture or only dynamics) is insufficient to trigger significant moisture convergence.

In conclusion, this paper constructs a physical mechanism model termed "Dual-Pathway Superposition" (illustrated in Figure 10). The summer extreme rainfall over the MLYR is triggered only when the tropical ocean-driven moisture pathway and the plateau-driven dynamic pathway coincide in space and time. This framework substantially refines our understanding of Asian monsoon predictability, emphasizing the necessity of considering both oceanic boundary forcing and internal atmospheric variability simultaneously.

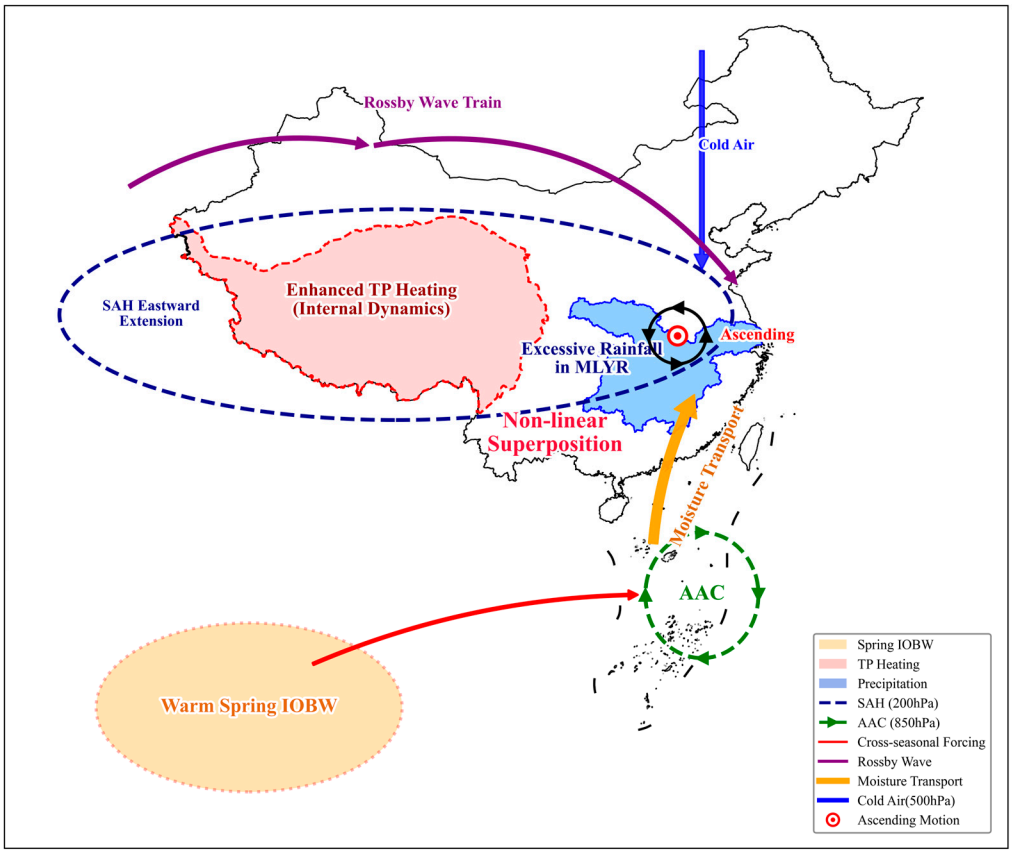

Figure 10. Schematic diagram of the "Dual-Pathway Superposition" mechanism driving extreme MLYR precipitation.

Author Contributions: Conceptualization, M.L. and Y.M.; methodology, M.L.; software, M.L.; validation, M.L., Y.M. and X.D.; formal analysis, Y.M.; investigation, M.L.; resources, Y.M. and X.D.; data curation, M.L., M.W., P.Y., Q.Z. and C.G.; writing—original draft preparation, M.L.; writing—review and editing, Y.M. and X.D.; visualization, M.L.; supervision, Y.M. and X.D.; project administration, Y.M.; funding acquisition, Y.M., M.L. and X.D. All authors have read and agreed to the published version of the manuscript.

Funding: This research was funded by the National Natural Science Foundation of China (Nos. 42230610, U2442213).

Institutional Review Board Statement: Not applicable.

Informed Consent Statement: Not applicable.

Data Availability Statement: The boundary of the MLYR can be obtained from the website http://www.geodata.cn/main/, accessed on 17 April 2026. The TP boundary can be obtained from the website https://data.tpdc.ac.cn/home, accessed on 17 April 2026. ERA5 data are at https://cds.climate.copernicus.eu/, accessed on 17 April 2026. CMIP6 AMIP model data are at https://aims2.llnl.gov/, accessed on 17 April 2026. The ERSST v5 data can be obtained from the website https://psl.noaa.gov/, accessed on 17 April 2026. The CN05.1 monthly precipitation data and observed data from 2400 stations in China are obtained by request and not publicly available.

Conflicts of Interest: The authors declare no conflicts of interest.

Abbreviations

The following abbreviations are used in this manuscript:

AAC	Anomalous Anticyclone
AMIP	Atmospheric Model Intercomparison Project
CMA	China Meteorological Administration
CMIP6	Coupled Model Intercomparison Project Phase 6
EASM	East Asian Summer Monsoon
ECMWF	European Centre for Medium-Range Weather Forecasts
ERA5	Fifth-generation global atmospheric reanalysis
ERSST	Extended Reconstructed Sea Surface Temperature
IOBW	Indian Ocean Basin Warming
IOC	Indian Ocean Capacitor
LH	Latent Heat Flux
MJO	Madden-Julian Oscillation
MLYR	Middle and Lower Reaches of the Yangtze River
MME	Multi-Model Ensemble
NOAA	National Oceanic and Atmospheric Administration
PC1	Principal Component 1
SAH	South Asian High
SCF	Squared Covariance Fraction
SH	Surface Sensible Heat Flux
SHAP	Sensible Heat Air Pump
SRP	Silk Road Pattern
SST	Sea Surface Temperature
SVD	Singular Value Decomposition
TP	Tibetan Plateau
WCRP	World Climate Research Programme
WPSH	Western Pacific Subtropical High

References

1. Ye, D.Z.; Wu, G.X. The role of the heat source of the Tibetan Plateau in the general circulation. *Meteorol. Atmos. Phys.* **1998**, *67*, 181–198. [CrossRef]
2. Wu, G.X.; Liu, Y.M.; He, B.; Bao, Q.; Duan, A.M.; Jin, F.-F. Thermal controls on the Asian summer monsoon. *Sci. Rep.* **2012**, *2*, 404. [CrossRef]
3. Fu, Y.F.; Ma, Y.M.; Zhong, L.; Yang, Y.J.; Guo, X.L.; Wang, C.H.; Xu, X.F.; Yang, K.; Xu, X.D.; Liu, L.P.; et al. Land-surface processes and summer-cloud-precipitation characteristics in the Tibetan Plateau and their effects on downstream weather: A review and perspective. *Natl. Sci. Rev.* **2020**, *7*, 500–515. [CrossRef]
4. Zhao, P.; Xu, X.D.; Chen, F.; Guo, X.L.; Zheng, X.D.; Liu, L.P.; Hong, Y.; Li, Y.Q.; La, Z.; Peng, H. The third atmospheric scientific experiment for understanding the earth–atmosphere coupled system over the Tibetan Plateau and its effects. *Bull. Am. Meteorol. Soc.* **2018**, *99*, 757–776. [CrossRef]
5. Liu, Y.M.; Wu, G.X.; Hong, J.L.; Dong, B.W.; Duan, A.M.; Bao, Q.; Zhou, L.J. Revisiting Asian monsoon formation and change associated with Tibetan Plateau forcing: II. change. *Clim. Dyn.* **2012**, *39*, 1183–1195. [CrossRef]
6. Wu, G.X.; Zhang, Y.S. Tibetan Plateau forcing and the timing of the monsoon onset over south Asia and the south China sea. *Mon. Weather Rev.* **1998**, *126*, 913–927. [CrossRef]
7. Hoskins, B.J.; Karoly, D.J. The steady linear response of a spherical atmosphere to thermal and orographic forcing. *J. Atmos. Sci.* **1981**, *38*, 1179–1196. [CrossRef]
8. Ding, Y.; Liu, Y.; Hu, Z.Z. The Record-breaking Mei-yu in 2020 and Associated Atmospheric Circulation and Tropical SST Anomalies. *Adv. Atmos. Sci.* **2021**, *38*, 1980–1993. [CrossRef] [PubMed]
9. Zhao, P.; Chen, L.X. Climatic features of atmospheric heat source/sink over the Qinghai-Xizang Plateau in 35 years and its relation to rainfall in China. *Sci. China Ser. D Earth Sci.* **2001**, *44*, 858–864. [CrossRef]
10. Duan, A.M.; Wu, G.X.; Liu, Y.M.; Ma, Y.M.; Zhao, P. Weather and climate effects of the Tibetan Plateau. *Adv. Atmos. Sci.* **2012**, *29*, 978–992. [CrossRef]

11. Zhang, L.X.; Zhao, D.; Zhou, T.J.; Peng, D.D.; Xiao, C. Moisture origins and transport processes for the 2020 Yangtze River valley record-breaking Mei-yu rainfall. *Adv. Atmos. Sci.* **2021**, *38*, 2125–2136. [CrossRef]
12. Pan, X.; Li, T.; Sun, Y.; Zhu, Z.W. Cause of extreme heavy and persistent rainfall over Yangtze River in summer 2020. *Meteorol. Atmos. Phys.* **2021**, *38*, 1994–2009. [CrossRef]
13. Liu, B.Q.; Yan, Y.H.; Zhu, C.W.; Ma, S.M.; Li, J.Y. Record-breaking Meiyu rainfall around the Yangtze River in 2020 regulated by the subseasonal phase transition of the north atlantic oscillation. *Geophys. Res. Lett.* **2020**, *47*, e2020GL090342. [CrossRef]
14. Kuang, X.X.; Jiao, J. Review on climate change on the Tibetan Plateau during the last half century. *J. Geophys. Res. Atmos.* **2016**, *121*, 3979–4007. [CrossRef]
15. Yao, T.D.; Bolch, T.; Chen, D.L.; Gao, J.; Immerzeel, W.; Piao, S.L.; Su, F.G.; Thompson, L.; Wada, Y.; Wang, L. The imbalance of the Asian water tower. *Nat. Rev. Earth Environ.* **2022**, *3*, 618–632. [CrossRef]
16. Sun, J.; Yang, K.; Guo, W.D.; Wang, Y.; He, J.; Lu, H. Why has the inner Tibetan Plateau become wetter since the mid-1990s? *J. Clim.* **2020**, *33*, 8507–8522. [CrossRef]
17. Yang, K.; Wu, H.X.; Qin, J.; Lin, C.G.; Tang, W.J.; Chen, Y.Y. Recent climate changes over the Tibetan Plateau and their impacts on energy and water cycle: A review. *Glob. Planet. Change* **2014**, *112*, 79–91. [CrossRef]
18. Duan, A.M.; Wu, G.X. Weakening trend in the atmospheric heat source over the Tibetan Plateau during recent decades. part I: Observations. *J. Clim.* **2008**, *22*, 3149–3164. [CrossRef]
19. Huang, J.P.; Zhou, X.J.; Wu, G.X.; Xu, X.D.; Zhao, Q.Y.; Liu, Y.M.; Duan, A.M.; Xie, Y.K.; Ma, Y.M.; Zhao, P. Global climate impacts of land-surface and atmospheric processes over the Tibetan Plateau. *Rev. Geophys.* **2023**, *61*, e2022RG000771. [CrossRef]
20. Wang, M.R.; Wang, J.; Chen, D.L.; Duan, A.M.; Liu, Y.M.; Zhou, S.W.; Guo, D.; Wang, H.M.; Ju, W.M. Recent recovery of the boreal spring sensible heating over the Tibetan Plateau will continue in CMIP6 future projections. *Environ. Res. Lett.* **2019**, *14*, 124066. [CrossRef]
21. Cui, Y.F.; Duan, A.M.; Liu, Y.M.; Wu, G.X. Interannual variability of the spring atmospheric heat source over the Tibetan Plateau forced by the north atlantic SSTA. *Clim. Dyn.* **2015**, *45*, 1617–1634. [CrossRef]
22. Liu, Y.M.; Bao, Q.; Duan, A.M.; Qian, Z.A.; Wu, G.X. Recent progress in the impact of the Tibetan Plateau on climate in China. *Adv. Atmos. Sci.* **2007**, *24*, 1060–1076. [CrossRef]
23. Lu, R.-Y.; Oh, J.H.; Kim, B.J. A teleconnection pattern in upper-level meridional wind over the north African and Eurasian continent in summer. *Tellus A Dyn. Meteorol. Oceanogr.* **2002**, *54*, 44–55. [CrossRef]
24. Enomoto, T.; Hoskins, B.J.; Matsuda, Y. The formation mechanism of the Bonin high in August. *Q. J. R. Meteorol. Soc.* **2003**, *129*, 157–178. [CrossRef]
25. Wang, B.; Bao, Q.; Hoskins, B.; Wu, G.X.; Liu, Y.M. Tibetan Plateau warming and precipitation changes in east Asia. *Geophys. Res. Lett.* **2008**, *35*. [CrossRef]
26. Han, Y.Z.; Ma, W.Q.; Yang, Y.X.; Ma, Y.M.; Xie, Z.P.; Sun, G.H.; Menenti, M.; Su, B. Impacts of the silk road pattern on the interdecadal variations of the atmospheric heat source over the Tibetan Plateau. *Atmos. Res.* **2021**, *260*, 105696. [CrossRef]
27. Xie, S.-P.; Hu, K.; Hafner, J.; Tokinaga, H.; Du, Y.; Huang, G.; Sampe, T. Indian Ocean Capacitor Effect on Indo–Western Pacific Climate during the Summer following El Niño. *J. Clim.* **2009**, *22*, 730–747. [CrossRef]
28. Tang, H.S.; Hu, K.M.; Huang, G.; Wang, Y.; Tao, W.C. Intensification and northward extension of northwest pacific anomalous anticyclone in El Niño decaying mid-summer: An energetic perspective. *Clim. Dyn.* **2022**, *58*, 591–606. [CrossRef]
29. Hu, J.; Duan, A. Relative contributions of the Tibetan Plateau thermal forcing and the Indian Ocean Sea surface temperature basin mode to the interannual variability of the East Asian summer monsoon. *Clim. Dyn.* **2015**, *45*, 2697–2711. [CrossRef]
30. Huang, G.; Qu, X.; Hu, K.M. The impact of the tropical Indian Ocean on South Asian High in boreal summer. *Adv. Atmos. Sci.* **2011**, *28*, 421–432. [CrossRef]
31. Xin, X.G.; Wu, T.W.; Zhang, J.; Yao, J.C.; Fang, Y.J. Comparison of CMIP6 and CMIP5 simulations of precipitation in China and the East Asian summer monsoon. *Int. J. Climatol.* **2020**, *40*, 6423–6440. [CrossRef]
32. Chen, H.P.; Sun, J.Q.; Lin, W.Q.; Xu, H.W. Comparison of CMIP6 and CMIP5 models in simulating climate extremes. *Sci. Bull.* **2020**, *65*, 1415–1418. [CrossRef]
33. Dong, T.Y.; Dong, W.J. Evaluation of extreme precipitation over Asia in CMIP6 models. *Clim. Dyn.* **2021**, *57*, 1751–1769. [CrossRef]
34. Wu, G.X.; Liu, Y.M.; Zhang, Q.; Duan, A.M.; Wang, T.M.; Wan, R.J. The Influence of mechanical and thermal forcing by the Tibetan Plateau on Asian climate. *J. Hydrometeorol.* **2007**, *8*, 770–789. [CrossRef]
35. Hersbach, H.; Bell, B.; Berrisford, P.; Hirahara, S.; Horányi, A.; Muñoz-Sabater, J.; Nicolas, J.; Peubey, C.; Radu, R.; Schepers, D.; et al. The ERA5 global reanalysis. *Q. J. R. Meteorol. Soc.* **2020**, *146*, 1999–2049. [CrossRef]
36. Wang, S.M.; Xu, T.H.; Nie, W.F.; Jiang, C.H.; Yang, Y.G.; Fang, Z.L.; Li, M.W.; Zhang, Z. Evaluation of precipitable water vapor from five reanalysis products with ground-based GNSS observations. *Remote Sens.* **2020**, *12*, 1817. [CrossRef]
37. Huang, L.K.; Mo, Z.X.; Liu, L.L.; Zeng, Z.L.; Chen, J.; Xiong, S.Q.; He, H.C. Evaluation of hourly PWV products derived from ERA5 and MERRA-2 over the Tibetan Plateau using ground-based GNSS observations by two enhanced models. *Earth Space Sci.* **2021**, *8*, e2020EA001516. [CrossRef]

38. Wu, J.; Gao, X.J. A gridded daily observation dataset over China region and comparison with the other datasets. *Chin. J. Geophys.* **2013**, *56*, 1102–1111. [CrossRef]
39. Huang, B.; Thorne, P.W.; Banzon, V.F.; Boyer, T.B.; Chepurin, G.; Lawrimore, J.H.; Menne, M.J.; Smith, T.M.; Vose, R.S.; Zhang, H.-M. Extended Reconstructed Sea Surface Temperature, Version 5 (ERSSTv5): Upgrades, Validations, and Intercomparisons. *J. Clim.* **2017**, *30*, 8179–8205. [CrossRef]
40. Eyring, V.; Bony, S.; Meehl, G.A.; Stevens, B.; Stouffer, R.J.; Taylor, K.E. Overview of the coupled model intercomparison project phase 6 (CMIP6) experimental design and organization. *Geosci. Model Dev.* **2015**, *9*, 1937–1958. [CrossRef]
41. Jiang, D.B.; Hu, D.; Tian, Z.P.; Lang, X.M. Differences between CMIP6 and CMIP5 models in simulating climate over China and the East Asian monsoon. *Adv. Atmos. Sci.* **2020**, *37*, 1102–1118. [CrossRef]
42. Ye, D.; Gao, Y. *Meteorology of the Qinghai-Xizang Plateau*; Science Press: Beijing, China, 1979.
43. Seager, R.; Naik, N.; Vecchi, G.A. Thermodynamic and dynamic mechanisms for large-scale changes in the hydrological cycle in response to global warming. *J. Clim.* **2010**, *23*, 4651–4668. [CrossRef]
44. Bretherton, C.S.; Smith, C.; Wallace, J.M. An Intercomparison of methods for finding coupled patterns in climate data. *J. Clim.* **1992**, *5*, 541–560. [CrossRef]
45. Welch, B. The generalisation of student's problems when several different population variances are involved. *Biometrika* **1947**, *34*, 28–35. [CrossRef]
46. Zhou, T.; Song, F.; Ha, K.-J.; Chen, X. Decadal change of East Asian summer monsoon: Contributions of internal variability and external forcing. In *The Global Monsoon System: Research and Forecast*; World Scientific: Singapore, 2017; pp. 327–336.
47. Huang, F.; Xu, Z.; Guo, W.; Feng, J.; Chen, L.; Zheng, H.; Fu, C. Relative contributions of internal variability and external forcing to the inter-decadal transition of climate patterns in East Asia. *npj Clim. Atmos. Sci.* **2023**, *6*, 21. [CrossRef]
48. Zhu, C.; Ullah, W.; Wang, G.; Lu, J.; Li, S.; Feng, A.; Hagan, D.F.T.; Jiang, T.; Su, B. Diagnosing potential impacts of Tibetan Plateau spring soil moisture anomalies on summer precipitation and floods in the Yangtze River basin. *J. Geophys. Res. Atmos.* **2023**, *128*, e2022JD037671. [CrossRef]
49. Zhang, C.; Jia, X.; Wen, Z. Increased impact of the Tibetan Plateau spring snow cover to the Mei-yu rainfall over the Yangtze River valley after the 1990s. *J. Clim.* **2021**, *34*, 5985–5997. [CrossRef]
50. Zheng, J.; Wang, C. Influences of three oceans on record-breaking rainfall over the Yangtze River Valley in June 2020. *Sci. China Earth Sci.* **2021**, *64*, 1607–1618. [CrossRef]
51. Zhong, S.; Wang, H.; Chen, B.; Chen, H. Modulation of the atmospheric heat source over the Tibetan Plateau on the intra-seasonal oscillation of summer precipitation in the Yangtze-Huaihe River Basin. *Atmos.-Ocean* **2022**, *60*, 600–612. [CrossRef]